Energy & Environmental Science

Machine Learning-Assisted Ultrafast Flash Sintering of High-Performance and Flexible Silver-Selenide Thermoelectric Devices

Journal:	*Energy & Environmental Science*
Manuscript ID	EE-ART-06-2022-001844.R2
Article Type:	Paper
Date Submitted by the Author:	20-Sep-2022
Complete List of Authors:	Saeidi-Javash, Mortaza; University of Notre Dame, Department of Aerospace and Mechanical Engineering Wang, Ke; University of Notre dame, Department of Chemical and Biomolecular Engineering Zeng, Minxiang; University of Notre Dame, Department of Aerospace and Mechanical Engineering Luo, Tengfei; University of Notre Dame, Aerospace and Mechanical Engineering Dowling, Alexander; University of Notre Dame, Chemical and Biomolecular Engineering Zhang, Yanliang; University of Notre dame, Department of Aerospace and Mechanical Engineering

Thermoelectric devices offer great opportunities in solid-state conversion of waste heat into electricity and refrigeration with no moving parts or environmental emission from refrigerants. To realize its broad applications in energy harvesting and cooling, significant advances are required to not only increase thermoelectric figure of merit zT but also improve the mechanical flexibility and reduce the manufacturing time and cost. While nanoscale materials offer opportunities to enhance zT by tailoring the electron and phonon transport, challenges still remain to process these nanoscale materials into high-performance and low-cost devices. Here we demonstrate a machine learning assisted high-throughput and ultrafast (< 1 second) photonic flash processing method that sinters silver-selenide nanoparticles into flexible films with room temperature zT > 1, which is among the highest in flexible thermoelectric materials. Bayesian optimization was applied to accelerate the discovery of the optimum manufacturing conditions using less than 40 experiments, despite the complexity of photonic flash sintering processes. The successful integration of high-throughput photonic flash processing and machine learning can be generalized to highly scalable and low-cost manufacturing of a broad range of energy and electronic materials.

Machine Learning-Assisted Ultrafast Flash Sintering of High-Performance and Flexible Silver-Selenide Thermoelectric Devices

Mortaza Saeidi-Javash,[a,c] Ke Wang,[b] Minxiang Zeng,[a,d] Tengfei Luo,[a,b] Alexander W. Dowling,[b] and Yanliang Zhang[a]*

[a] Department of Aerospace and Mechanical Engineering, University of Notre Dame, Notre Dame, IN 46556, USA

[b] Department of Chemical and Biomolecular Engineering, University of Notre Dame, Notre Dame, IN 46556, USA

[c] Department of Mechanical and Aerospace Engineering, California State University Long Beach, Long Beach, CA 90840, USA

[d] Department of Chemical Engineering, Texas Tech University, Lubbock, TX 79409, USA

*Corresponding Author: yzhang45@nd.edu

Keywords:

Flash sintering, machine learning, Bayesian optimization, thermoelectric films, silver-selenide

1. Abstract

Flexible thermoelectric generators (TEGs) have shown immense potential for serving as a power source for wearable electronics and Internet of Things. A key challenge preventing large-scale applications of TEG lies with the lack of high-throughput processing method which can sinter thermoelectric (TE) materials rapidly while maintaining their high thermoelectric properties. Herein, we integrate high-throughput experimentation and Bayesian optimization (BO) to accelerate the discovery of the optimum sintering conditions of silver-selenide TE films using an ultrafast intense pulsed light (flash) sintering technique. Due to the nature of high-dimension

optimization problem of flash sintering processes, a Gaussian Process Regression (GPR) machine learning model is established to rapidly recommend the optimum flash sintering variables based on Bayesian expected improvement. For the first time, an ultrahigh power factor flexible TE film (power factor of 2205 $\mu W/mK^2$ with zT of 1.1 at 300 K) is demonstrated with a sintering time less than 1.0 second, which is several orders of magnitude shorter than conventional thermal sintering techniques. The films also show excellent flexibility with 92% retention of the power factor (PF) after 10^3 bending cycles with a 5 mm bending radius. In addition, a wearable thermoelectric generator based on the flash sintered films generates a very competitive power density of 0.5 mW/cm^2 at a temperature difference of 10 K. This work not only shows tremendous potential of high-performance and flexible silver-selenide TEGs, but also demonstrates a machine learning-assisted flash sintering strategy that could be used for ultrafast, high-throughput and scalable processing of functional materials for a broad range of energy and electronic applications.

2. Introduction

Flexible Thermoelectric Generators (TEGs) are promising candidates for developing self-powered wearable devices and industrial Internet of Things.[1–5] Flexible TEGs are lightweight, compact, and maintenance-free solid-state energy convertors with no moving parts that directly convert heat into electricity, and they can easily conform to a variety of heat sources with curved surfaces (e.g., body heat). The efficiency of thermoelectric (TE) materials largely depends on the dimensionless figure of merit (zT) defined as $zT = \frac{\sigma S^2}{\kappa} T$ where S, σ, κ, and T denote the Seebeck coefficient, electrical conductivity, thermal conductivity, and absolute temperature, respectively.[6–8] Despite the significant progress in thermoelectric materials to date, Bi_2Te_3-based alloys remain as dominant materials for thermoelectric applications near room temperature, and the zT for n-type TE materials still remains below or around unity at room temperature.[6,9,10] In addition, the scarcity of tellurium (Te) necessitates the development of new tellurium-free thermoelectric materials for use in widespread industrial and wearable applications. Silver-selenide (Ag_2Se) is a narrow band gap n-type chalcogenide and an ideal candidate for room temperature applications owing to its high power factor (PF) and low intrinsic thermal conductivity.[11–20]

Sintering is an essential step in materials processing to improve transport properties. Sintering transforms TE particles into a dense structure with improved thermoelectric properties. Conventional thermal sintering requires hours of processing time at elevated temperatures which hinders the widespread development of flexible TEGs on organic substrates of low melting point (e.g., polymers, fabrics). In addition, it hampers the high-throughput discovery and energy-efficient manufacturing of high-performance TE materials with optimized compositions. Substantial effort has been devoted to the development of innovative sintering methods, such as

microwave-assisted sintering, spark plasma sintering (SPS), chemical sintering, and intense pulsed light (flash) sintering.[21–29] Among these techniques, flash sintering using intense pulsed light is uniquely advantageous. For example, it is ultrafast, energy-efficient, and can sinter the TE films at elevated temperatures on low melting point substrates without damaging the underneath substrate. Although flash sintering has been used for a variety of conductive materials such as silver, copper, and graphene, it remains relatively underexplored on semiconducting nanomaterials, particularly TE materials.[28–32] Sintering of TE nanoparticles constitutes a complex process involving solvent evaporation, decomposition of organic ingredients, formation of inter-particle conduction pathways, and densification which highlights the imperative role of optimized flash sintering variables on the resulted TE properties.

Previous efforts to discover the optimum flash sintering variables relied on expert-driven Edisonian trial-and-error search which is time and labor intensive.[32] Enabled by recent advances in machine learning, data-driven approaches such as Bayesian optimization (BO) have rapidly permeated many fields including TE materials,[33–35] smart manufacturing,[36–38] and molecular modeling of chemical products.[39,40] Novel artificial intelligence (AI) systems enable automated prediction and optimization of materials and additive manufacturing processes.[33,36–38] Moreover, machine learning algorithms can both help intelligently maximize specific performance metrics as well as aid the revealing of the underlying physical mechanisms. While classical statistical design of experiments (e.g., full/partial factor design, response surface methods, ANOVA analysis) has been used to improve TE materials and manufacturing,[41–43] these approaches require experimental designs to be fixed at the beginning of an optimization iteration and the experimental design cannot be updated as new data become available during the optimization iteration. This is inefficient and

requires many experiments to optimize multiple factors simultaneously. BO overcomes these limitations by adaptively determining a sequence of experiments without assuming a parametric model for the data. In BO, the non-parametric GPR model is updated after each experiment is completed such that decisions are made based on all of the available data. For this reason, BO is replacing response surface design of experiments methods as the state-of-the-art for statistical optimization of laboratory experiments.[44,45]

Despite the renewed interest and recent success of AI and machine learning, there are often significant barriers in translating these methods into new application domains. In this work, we integrate, for the first time, flash sintering with a Gaussian Process Regression (GPR) machine learning model and BO to predict the optimum flash sintering variables for n-type silver-selenide TE films that leads to maximum PF at room temperature. The proposed methodology successfully optimized four sintering variables – voltage, pulse duration, number of pulses, and pulse delay time – resulting in a PF of 2205 $\mu W/mK^2$, and a corresponding zT of 1.1 at room temperature (among the highest in the reported flexible TE films) with a sintering time less than 1.0 second after only 32 experiment-machine learning iterations. This methodology could be easily generalized to ultrafast and high-throughput flash sintering of a diverse range of energy and electronic materials, as well as other manufacturing processes in general.

3. Results and Discussion

Figure 1 depicts our machine learning-assisted workflow to find the optimum flash sintering variables for silver-selenide TE films fabricated using vacuum-assisted filtration technique. The aim of the framework is to find a set of variables including voltage, pulse duration, number of

pulses, and pulse delay that yields the maximum power factor with a minimum number of experimental iterations. The workflow starts by flash sintering of silver-selenide films, then measuring the power factor of the films (**Figure 1**). The sintering variables and measured power factor is then used as an input for BO to predict the next set of variables to test.

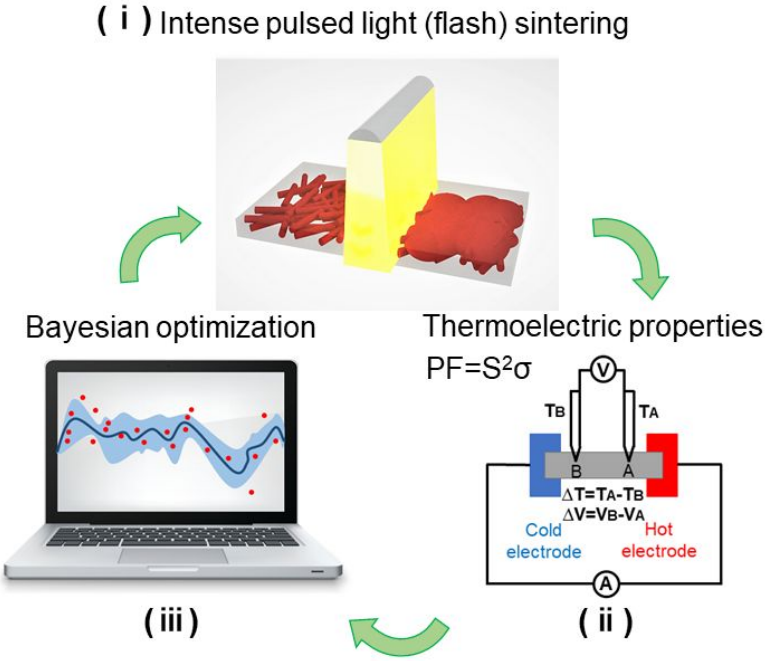

Figure 1. Schematic workflow of the machine learning-assisted flash sintering of silver-selenide TE films. **(i)** Intense pulsed light (flash) sintering. **(ii)** Thermoelectric properties measurement of the sintered film including the electrical conductivity, and the Seebeck coefficient. **(iii)** Bayesian optimization algorithm for the evaluation and suggestion of new sintering variables (voltage, pulse duration, number of pulses, and pulse delay) to test.

The preparation of silver-selenide nanostructures was based on the process reported in previous works.[11,20] Details of the synthesis is provided in the Materials and Methods section and **Figure S1**. The as-prepared products were dispersed in ethanol by sonication, and then deposited on a flexible porous filtration membrane with an average pore diameter of 0.22 μm (Tisch Scientific) by vacuum filtration. The as-prepared films were dried in vacuum and then cold-pressed at 25 MPa

for 15 min prior to flash sintering (**Figure S2**). During the fabrication process, the film thicknesses were controlled by the silver-selenide particle concentration (**Figure S3**). The structure and phase composition of the as-prepared silver-selenide powder was characterized by X-ray diffraction (XRD). **Figure S4(a)** displays the XRD pattern of the synthesized silver-selenide nanostructures before flash sintering. All the peaks in the pattern can be indexed to orthorhombic silver-selenide (JCPDF 24-1041), indicating there is no obvious impurities.[46] **Figure S4(b-c)** shows surface SEM images of the fabricated film before sintering, exhibiting a porous microstructure with randomly distributed silver-selenide nanostructures with diameters in the range of 50-200 nm.

Figure 2 shows the TE properties, and microstructure of the films under different sintering conditions listed in **Table S1**. Details of the TE properties measurement process is described in the Materials and Methods section. Overall, 37 experiments with unique set of sintering variables were tested, and three films were sintered under each condition to ensure the reproducibility of the results. The SEM-EDS map of element distribution of unsintered silver-selenide film confirms the Ag/Se molar ratio of 1.9:1 (see **Figure S5** and **Table S2**). A previous study has shown that adding small excess of anion (Se) to the stoichiometric composition leads to significant increase in power factor over stoichiometric Ag_2Se.[47] This extra Se significantly enhances carrier mobility and inhibits the formation of the metastable structure. Thus, we synthesized silver-selenide nanostructures with ~5% excess in selenium ($Ag_{1.9}Se$) to maximize the power factor. The silver-selenide films were fabricated in eight different thicknesses (16.5 μm, 14.3 μm, 13.3 μm, 9.0 μm, 3.8 μm, 2.7 μm, 2.4 μm, and 2.3 μm) and were classified in two general groups. Experiments 1 to 22 and 23 to 37 were conducted with films with average general thicknesses of 12.5 ± 3.2 μm, and 2.6 ± 0.5 μm, respectively (**Table S1**).

The typical light emission from the flash lamp (Xenon, type C) is within 200-700 nm. Room temperature in-plane TE properties of the sintered films are shown in **Figures 2(a)-(b)**. Sintered films under the BO optimized variables in experiment 32 (2.3 kV, 1.5 ms pulse time, 4 pulses, and 293 ms pulse delay) led to the Seebeck coefficient, and electrical conductivity of -161.7 μV/K, 8.4×10^4 S/m respectively with a maximum PF of 2205 ± 73.1 μW/mK^2 at room temperature which is among the highest in the reported flexible TE films and comparable to that of the bulk Ag_2Se.[16,48–50] It is worth noting that the total sintering time was less than a second where conventional thermal sintering usually takes 30 min or more (**Table 1**).

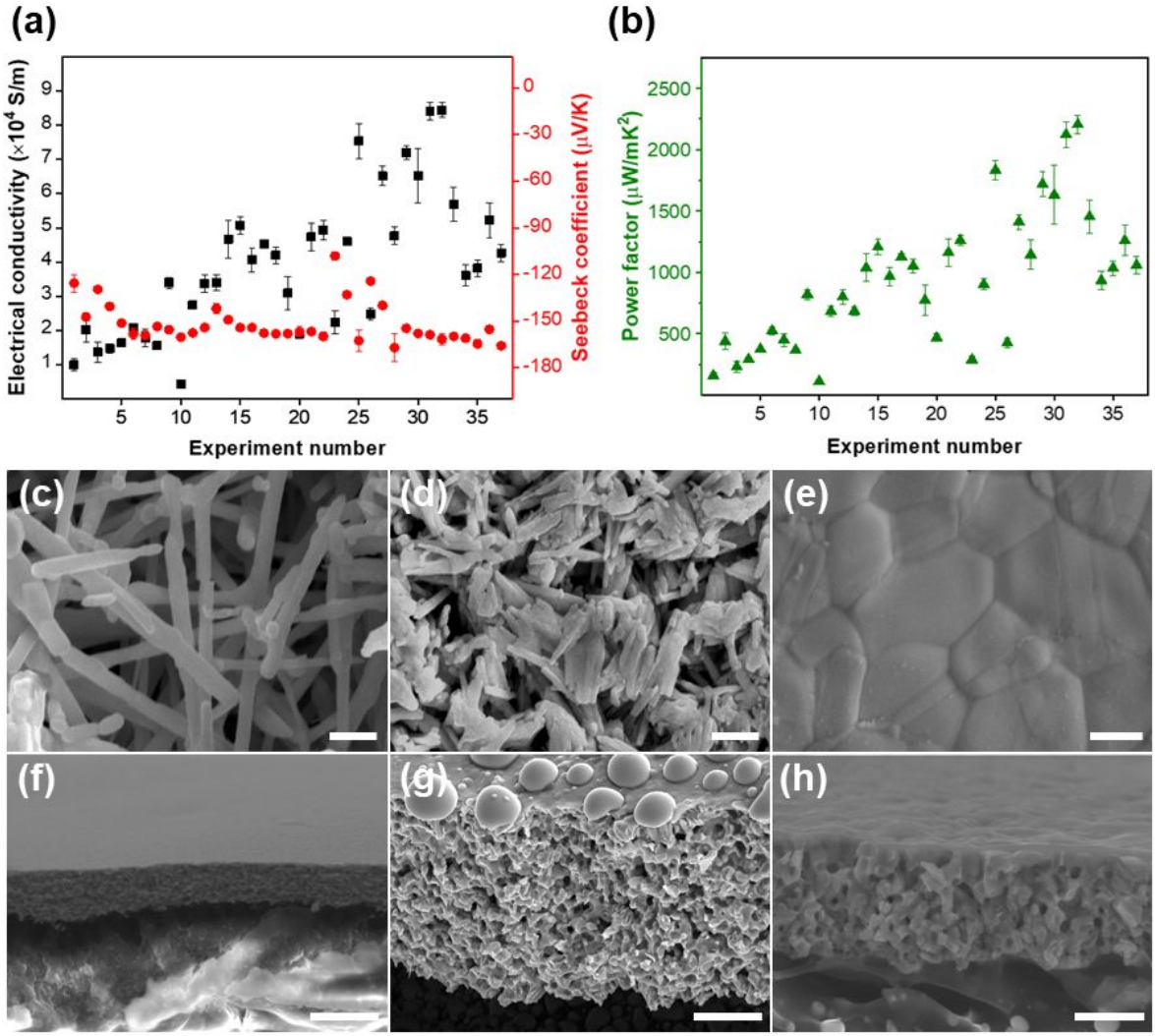

Figure 2. Room temperature in-plane TE properties of flash sintered silver-selenide TE films under different sintering conditions (details of each experiment and sintering variables are summarized in **Table S1**). **(a)** The electrical conductivity, and the Seebeck coefficient. **(b)** Power factor. Surface SEM images showing **(c)** unsintered silver-selenide film, **(d)** flash sintered film under non-optimum sintering variables (experiment 24) **(e)** flash sintered film under optimized sintering variables (experiment 32). Scale bars are 500 nm. Cross-sectional SEM images of **(f)** unsintered film. Scale bar is 5 μm. **(g)** The film with 14.3 μm thickness (experiment 6). Scale bar is 5 μm. **(h)** The film with 2.3 μm thickness (experiment 28). Scale bar is 2 μm.

Figures 2(c)-(e) demonstrate the surface SEM images of unsintered film, and flash sintered films with a representative non-optimum (experiment 24), and the optimum (experiment 32) variables. As shown in **Figure 2(c)** unsintered silver-selenide nanostructures are randomly distributed with a porous microstructure and limited carrier mobility which result in very low PF of 101.3 $\mu W/mK^2$. A single pulse with a deposited energy of ~1 J (experiment 24) on the film causes coarsening and grain size growth leading to an improved PF of 813.9 $\mu W/mK^2$ (**Figure 2(d)**). With optimized sintering variables and input energy (experiment 32), the grain size grows, and porosity decreases, which results in the maximum PF and almost 22-fold enhancement compared to the unsintered film (**Figure 2(e)**). It is worth mentioning that the thickness of silver-selenide films in experiments 32 and 24 is 2.4 μm and 2.3 μm, respectively; however, the optimal input energy in experiment 32 is 6.9 J which is almost 7-fold higher compared to experiment 24 (**Table S1**). This highlights the impact of optimal sintering conditions on TE properties. The corresponding TE properties of the SEM images are shown in **Figure S6**.

Hall effect measurements were carried out to provide insight into the charge carrier transport behavior of the flash sintered films. As shown in **Table S3**, the carrier mobility μ increases dramatically from 64.9 in unsintered film to 721.3 $cm^2\ V^{-1}\ s^{-1}$ in the sintered film under the optimized condition (experiment 32). Here, the increased mobility can be ascribed to the increased film density and grain sizes with decreased grain boundaries, as shown in Figure 2(e). The

decreased carrier concentration in the sintered film explains the increase of Seebeck coefficient after flash sintering. EDS analysis on sintered films under the optimized condition revealed a slight shift in composition from $Ag_{1.9}Se$ (unsintered film) to $Ag_{1.96}Se$ (**Table S4**). In addition, we conducted XRD analysis on silver-selenide films before and after flash sintering (experiment 32). The increase in X-ray diffraction intensity (**Figure S7**) indicates an improvement of crystallinity due to grain growth, which is consistent with the observation in SEM analysis. The unsintered sample shows weak characteristic peak of (112) and (121) of silver-selenide as well as wide peaks near 16^o to 26^o, of which the latter may correspond to the polymer substrate of the vacuum filtrated films. The sintered film also reveals almost identical phase with the bulk silver-selenide crystal in the Inorganic Crystal Structure Database (ICSD#52603), indicating no obvious impurities.

In addition, we found that the thicknesses of silver-selenide films played an important role in flash sintering process and the resulting TE properties. **Figures 2(f)-(h)** show cross-sectional SEM images of unsintered, and sintered films under the same input energy but with varying thicknesses. As shown in **Figure S8**, sintering films under the same input energy of ~2.54 J (experiments 6, and 28) but varying thicknesses of 14.3 μm and 2.3 μm results in PF of 523.5 $\mu W/mK^2$ and 1145.2 $\mu W/mK^2$ respectively. The films with reduced thicknesses undergo more uniform heating and sintering across the entire thickness, thus possessing the potential to achieve greater PF using the flash sintering (**Figures 2(g) and (h)**). Room temperature TE properties (**Figure S8**) show a 128% enhancement of the electrical conductivity under the same input energy by reducing thickness. We observed that an excessive input energy on thin films could cause sublimation of the silver-selenide nanostructures and create disconnected and porous microstructures with very low PF (see **Figure S9**).

Among the optimized sintering variables, pulse delay time between two adjacent pulses does not alter the input energy, but it impacts the microstructure and the resulted TE properties of the sintered films. **Figure S10** shows the room temperature TE properties of the films under three sets of sintering variables with the same input energy for each set but different pulse delay times. We found that the PF increased with decreasing pulse delay time. For example, decreasing the pulse delay time from 1500 ms to 248 ms in experiments 13 and 15 (details in **Table S1**), respectively, led to 76.7% increase in PF. This is attributed to elevated temperatures because of decreased pulse delay time between adjacent pulses that leads to densified microstructures.[51] This phenomenon was also observed for other TE material system (n-type $Bi_2Te_{2.7}Se_{0.3}$) in our previous study.[32]

The thermal diffusivity of the silver-selenide film was measured using the Angstrom method, and the in-plane thermal conductivity κ was determined using the relationship $\kappa = \alpha\rho c_p$ where α, c_p, and ρ are thermal diffusivity, specific heat capacity, and density, respectively. The in-plane κ of the silver-selenide films is 0.5 W/mK before sintering. The in-plane κ increases to 0.61 W/mK under the optimized sintering condition (experiment 32), which leads to a zT value of 1.1 at room temperature. As shown in **Figures 2(h)**, **S11**, and **S12,** the sintered film contains numerous pores of different sizes, which can effectively scatter phonons with short to long wavelengths and reduce lattice thermal conductivity. Details of the thermal diffusivity measurement process is described in Materials and Methods section, and Supplementary Information.

Figure 3 demonstrates and explains the efficacy of the GPR machine learning model to predict the PF of flash sintered films as a function of four sintering variables (voltage, pulse duration, number of pulses, pulse delay) and the thickness of the silver-selenide films.

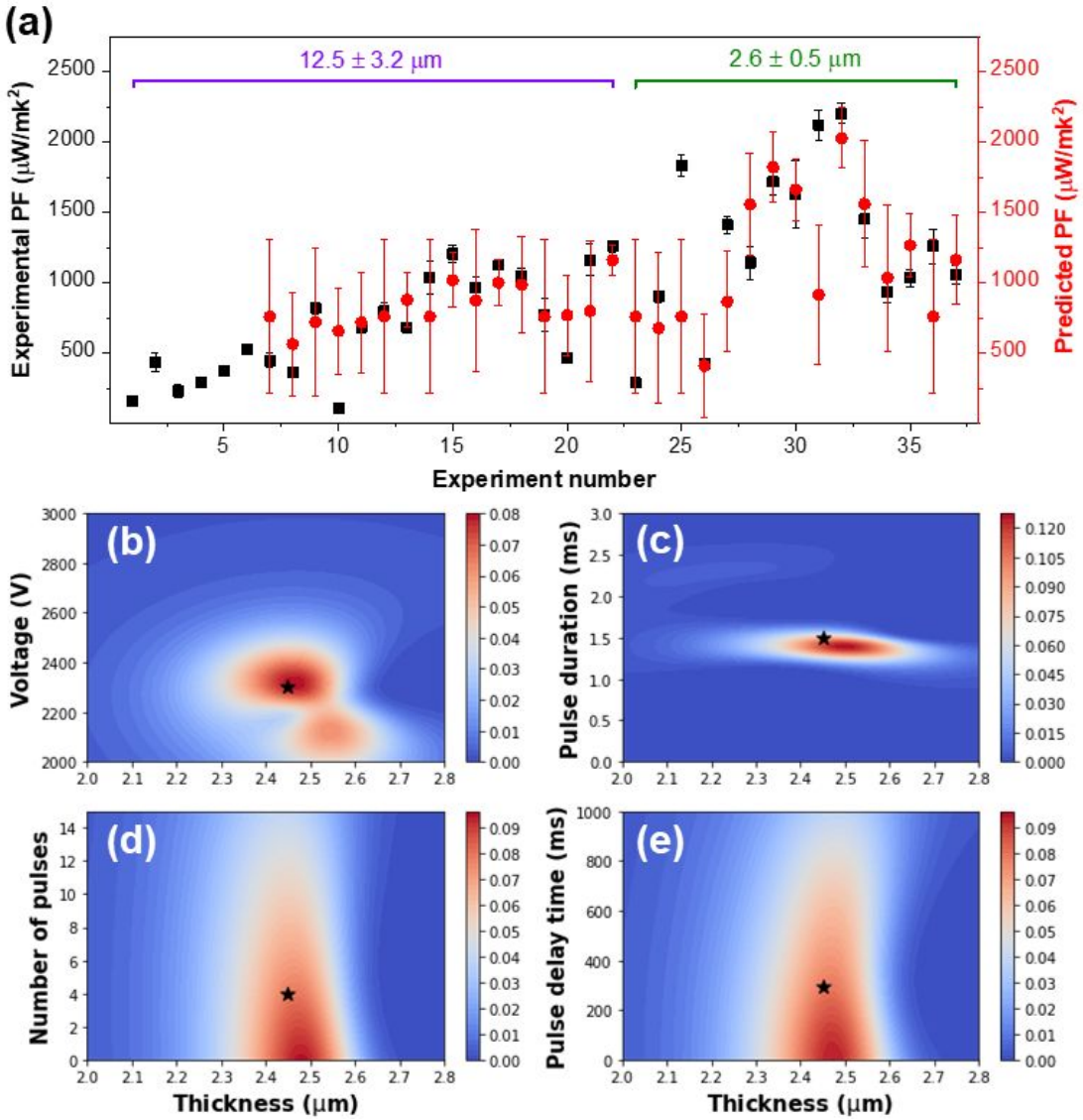

Figure 3. (a) Comparison of the measured and machine learning predicted power factors for sintered films. The red dots and error bars correspond to the GPR prediction mean and standard deviation. The black squares and error bars show the measured power factor. **(b)-(e)** Heatmaps show the sensitivity of the expected improvement (BO objective) as a function of thickness and **(b)** voltage, **(c)** pulse duration, **(d)** number of pulses, and **(e)** pulse delay time. The color scale from blue to red shows the expected improvement, where the red region indicates the range of optimal sintering variables. The black star marks the conditions of experiment 32 which had the maximum measured power factor.

The predicted power factors in **Figure 3(a)** are generated iteratively (with constant hyperparameters) using data from the prior experiments. For example, the GPR prediction for experiment 7 uses data from the six prior experiments for training. Out of the five variables, the four sintering variables can be controlled by adjusting the flash sintering processing parameters, while the film thickness can be controlled by adjusting the silver-selenide particle concentration during the vacuum filtration process. **Table S1** further divides the two groups of samples shown in Figure 3(a) with average thicknesses of 2.6 μm to 12.5 μm into eight subgroups. Analysis of **Figure 3(a)** and **Table S1** shows the GPR rapidly learns the process-property relationship and only needs one or two experiments in each thickness subgroup to make confident predictions on experiment with close distance (as explained in the Materials and Methods section, each prediction is a "weighted sum" of prior experiments). For example, experiments 14 to 22 are in the 9 μm thickness subgroup; experiment 14 has high prediction uncertainty of ±545 $\mu W/mK^2$ as there is no prior experimental data for a sample with 9 μm. Experiment 15 has close distance with experiment 14; thus, after incorporating experiment 14 in the GPR model, the prediction uncertainty of experiment 15 reduced to ±192 $\mu W/mK^2$. Experiment 16 is far away in distance compared with both experiment 14 and 15, leading to high prediction uncertainty of ±508 $\mu W/mK^2$; comparing experiment 16 with experiment 14, the prediction uncertainty decreased 6.7% because the prior experiments 14 and 15 enhance the confidence of the GPR model. As more data are added to each thickness subgroup near the optimal sintering conditions, one expects the GPR prediction uncertainty to converge to the experimental measurement uncertainty. In addition, **Table S1** includes data for 8 experiments in which the thin film burned, due to the excessive energy input, and the PF was measured to be zero. These experiments are not shown in **Figure 3(a)** for clarity but were included in the GPR analysis. Inspecting the GPR hyperparameters, $l_1 = 0.625$ (voltage),

$l_2 = 0.459$ (pulse duration), $l_3 = 5$ (number of pulses), $l_4 = 2.36$ (pulse delay), and $l_5 = 0.0477$ (thickness), reveals that the film thickness can influence effectiveness of the flash sintering process (as explained in the Materials and Methods section, the importance of a feature is inversely proportional to its length scale l) and the thinner films typically have higher PF comparing similar thicker films. As aforementioned, the films with reduced thicknesses experience more uniform heating and sintering across the entire thickness, leading to dense microstructure, and greater PF. These GPR results motivated the team to prepare the second group of thinner films shown in Figure 3(a), which underscores the synergies between experiments and machine learning modeling. **Figures 3(b)-(e)** show the sensitivity of the expected improvement metric (objective for BO) as a function of thickness and the other four flash sintering variables. **Figure S13** in the Electronic Supplementary Information shows similar heatmaps for the prediction mean, prediction uncertainty, and expected improvement over a wider thickness range (1 to 16 μm). These heatmaps confirm that the GPR model predicts a narrow thickness range, 2.2 μm to 2.6 μm, which maximizes the expected improvement. Moreover, **Figures 3(b)-(e)** and **Figure S13** show voltage and pulse duration are important factors on PF. Similarly, there is a wide range of pulse delay time and number of pulses that give a high expected improvement. This finding is consistent with importance of features indicated by the length scales as well as the Pearson correlation matrix shown in **Figure S14**. Furthermore, the gradual improvement in PF in each thickness group emphasizes the importance of optimizing all flash sintering variables. In this application, the film thickness was determined by the vacuum filtration process. The GPR model was then used to optimize the remaining four sintering variables with the thickness held constant.

A key contribution of this work is the integration of BO recommendations and expert intuition to maximize the PF of flash sintered silver-selenide TE films. To illustrate this integration, consider the results from experiments 23 to 30 in the second thickness group (2.6 ± 0.5 μm). Experiment 23 is chosen by intuition from previous experiments 1 to 22 as it is the first experiment in 2.3 μm thickness subgroup. The GPR was then updated to incoporated the result from experiment 23 and BO recommend up to five optimal conditions for the next experiment, which were then downselected by the experimental expert. Following this same procedure, the conditions for the next eight experiments (24 to 32) were chosen, resulting in the steady increase in power factor. The maximum PF was achieved at experiment 32 (see details of sintering conditions in **Table S1**) which is the final experiment in the sixth thickness subgroup (2.4 μm). We observed that the PF decreases for all subsequent five sintering experiments which correspond to seventh and eighth thickness subgroups (2.7 and 3.8 μm, respectively). One possibility, suggested by **Figure 3(b)-3(e)**, is that there is a narrow range of thickness values, approximately 2.3 to 2.6 μm for which the PF is maximized. The final five experiments (and two thickness subgroups) are outside this range.

Table 1 lists room temperature TE properties of several reported works on organic and inorganic TE materials including flexible silver-selenide films fabricated using vacuum-assisted filtration method. Our approach using machine learning for optimizing the flash sintering process not only results in an ultrahigh PF and zT, among the highest in n-type flexible TE materials, but also significantly decreases the sintering time to less than one second.

Table 1. Room temperature TE properties of organic and inorganic TE materials including silver-selenide films with different compositions.

Composition	Sintering time (s)	Seebeck coefficient (μV/K)	Electrical conductivity (S/m)	Thermal conductivity (W/mK)	Power factor (μW/mK^2)	zT	Ref.
$Cu_1Ag_4Se_3$	1800	-45.7	7.6×10^4	1.32	1594	0.4	11
PVP-Ag_2Se	1800	-143.4	9.3×10^4	0.51	1910	1.1	12
Ag_2Se	1800	-143.0	9.2×10^4	0.69	1882	0.8	13
$Ag_{1.8}Se$	1800	-120.3	6.7×10^4	NA	975*	NA	17
Ag_2Se/Se/polypyrrole	1800	-144.0	10.6×10^4	0.71	2240	0.9	19
β-Ag_2Se	1800	-140.7	4.9×10^4	0.48	987	0.6	20
$Sb_{1.6}Bi_{0.4}Te_3$/Te	2700	204	7.2×10^4	0.9	3000	1	52
Sb_2Te_3/Te	3600	130	7.8×10^4	NA	1370	NA	53
Te/PEDOT	600	115	2.1×10^4	0.22	284	0.39	54
CNT/PANI	72000	61	6.1×10^4	0.7	220	0.1	55
Bi_2Te_3	600	-141	6.7×10^4	1.2	1332	0.3	56
$Bi_2Te_{2.7}Se_{0.3}$	1.5	-163	2.7×10^4	NA	730	NA	32
$Ag_{1.96}Se$	< 1	-161.7	8.4×10^4	0.61	2205	1.1	**This work**

*Digitized from the reference.

Apart from the TE properties, the flexibility and mechanical durability of the silver-selenide films play a vital role in fabricating flexible TEGs for practical applications (e.g., wearable electronics). **Figure 4** demonstrates the average ratio of the electrical conductivity (σ/σ_0), Seebeck coefficient (S/S_0), and power factor (PF/PF_0) as a function of bending cycles. Three samples were tested, and the error bar represents the standard deviation from these samples. We used a programmable linear motion slide for the bending test with a bending radius of 5 mm. **Figure S15** demonstrates the film

under different bending angels. As shown in Figure 4, the electrical conductivity decreases slightly with the increasing of bending cycles whereas the Seebeck coefficient is almost stable. This leads to about 8% decrease in PF after 10^3 bending cycles which confirms the excellent flexibility and robustness of the sintered films. **Table S5** lists flexibility of several recently reported works on silver-selenide films fabricated using vacuum-assisted filtration method.

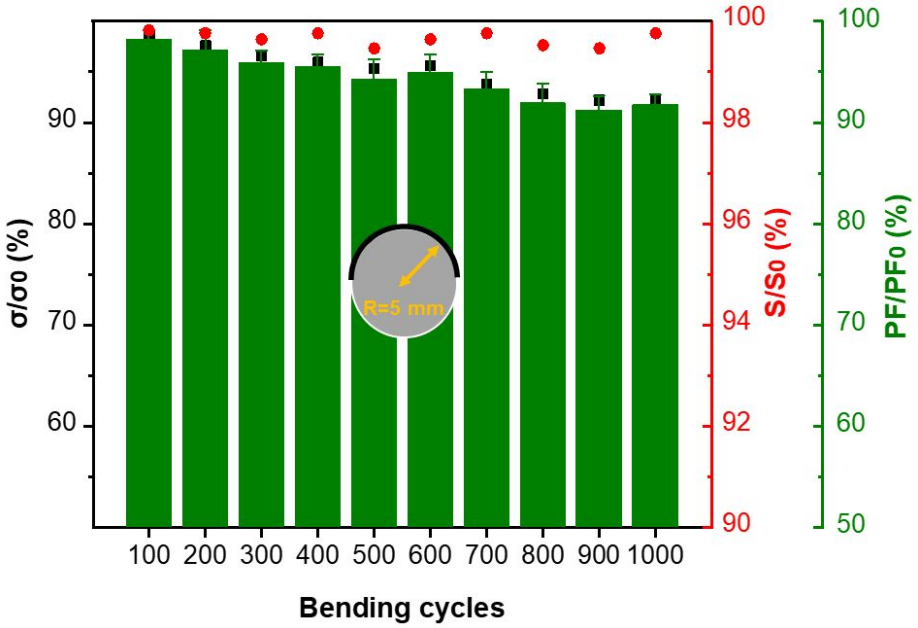

Figure 4. Flexibility test of the flash sintered films. The electrical conductivity, the Seebeck coefficient, and the PF change of the films after bending for 1000 cycles. Bending radius is 5 mm.

A flexible TEG was assembled with six silver-selenide legs sintered under the optimum condition (experiment 32: 2.3 kV voltage, 1.5 ms pulse duration, 4 pulses, and 293 ms pulse delay time) with internal resistance of 75.8 Ω. **Figure S16** demonstrates the fabricated TEG and the measurement setup. Details are included in the Materials and Methods section. The theoretical internal resistance of the six silver-selenide legs is calculated to be 75.4 Ω using the resistivity and the dimensions of the TE legs, which is in good agreement with the measured internal resistance. The small difference (<0.5%) between the measured and the theoretical resistances is attributed to the silver electrodes and the contact resistance between the TE legs and silver electrodes. **Figure 5(a)** shows

the measured device open circuit voltage (V_{oc}) under different temperature gradients up to 70 K. The measured values are almost equal to the theoretical values which are calculated according to the expression V_{oc} =N|S|ΔT where N is the number of TEG legs, S is the Seebeck coefficient, and ΔT is the corresponding temperature gradient with the maximum output voltage of 67.5 mV at ΔT of 70 K.

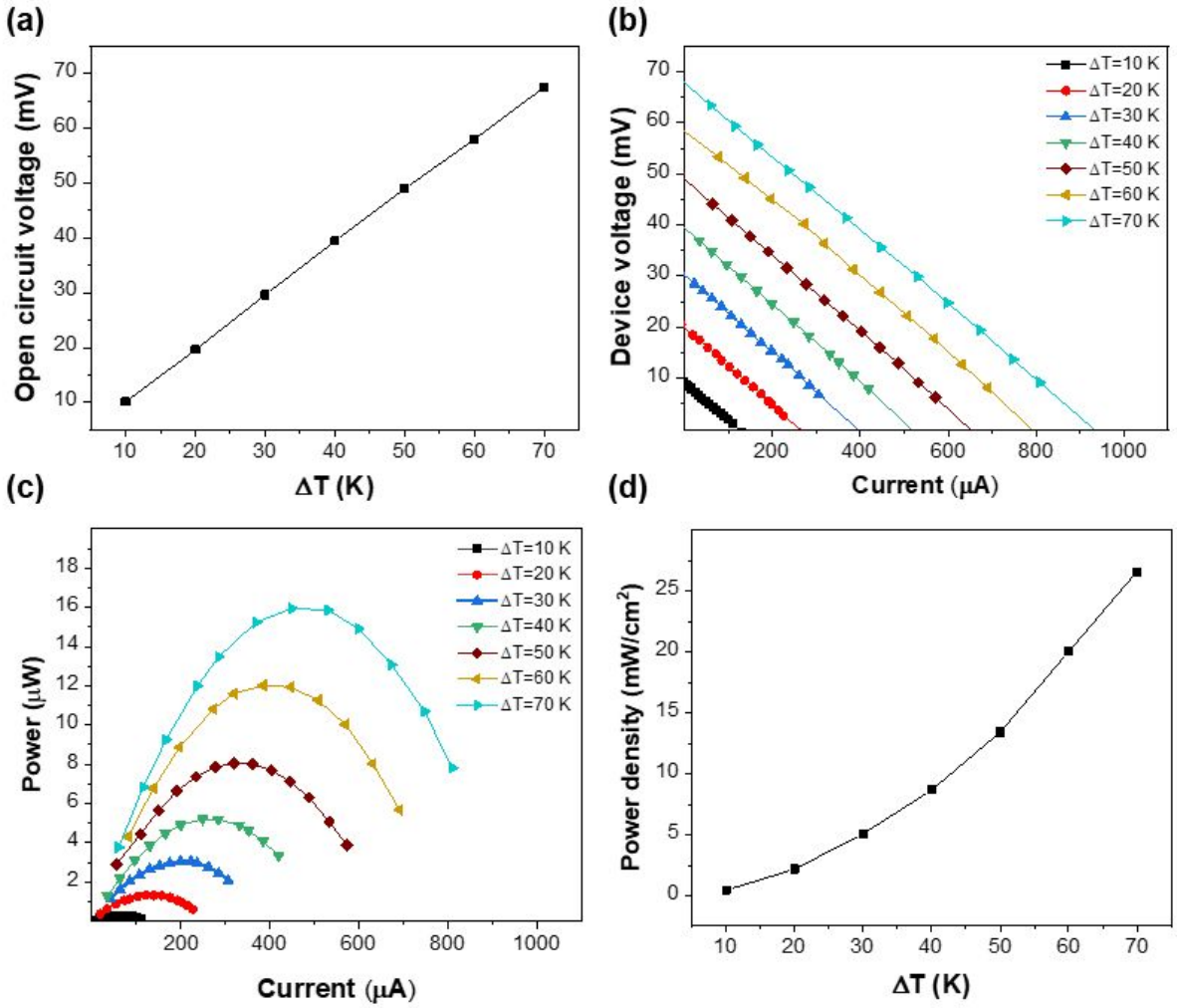

Figure 5. Performance of a flexible TEG fabricated using flash sintered silver-selenide films. **(a)** Open-circuit voltage at different temperature gradients. **(b)** Device operating voltage versus current at various ΔT. **(c)** Power output versus electrical current. **(d)** Electrical power density at various ΔT.

Figure 5(b) shows the device operating voltage as a function of electrical current where there is a linear negative correlation between the output voltage and the output current. **Figure 5(c)** shows

the device power output at different ΔT with the maximum power output of almost 16 μW at ΔT of 70 K. As conventionally calculated,[11,13,57] the power density can be obtained from dividing the generated power by the number of legs N and the cross-sectional area $A = w \times t$, where w is the width of films and t is the thickness of silver-selenide film. As shown in **Figure 5(d)**, the maximum power density is calculated to be 0.5 and 26.6 mW/cm^2 at ΔT of 10 and 70 K, respectively. This is sufficient to power a variety of low energy consumption Internet of Things sensors. In addition, we demonstrated a wearable TEG to harvest heat from human body and convert it to electricity. **Figure 6** shows the flexible TEG with internal resistance of 56 Ω was tied around an arm with a generated voltage of 1.4 mV at ΔT of ~1.8 K between the hot-side and the cold-side of the device.

Figure 6. Performance of a wearable TEG. **(a)** Internal resistance of the TEG fabricated using six silver-selenide films. **(b)** The digital photo of 1.4 mV open-circuit voltage generated by ΔT of ~1.8 K between the hot-side and the cold-side of the device. The inset is the corresponding infrared thermal image.

We also tested the stability of the TEG by exposing it to the air for a month and monitored the internal resistance change over time. After being exposed to air, the internal resistance of the device increased by ~0.5% to 76.2 Ω, showing an excellent stability of the sintered silver-selenide films even without encapsulation. The flexible TEG can be applied to energy harvesting from other

heat sources with higher temperatures than human body, such as power plants, factories, industrial machines, geothermal and other low-grade waste heat sources. In addition to energy harvesting, an alternative application could be thermoelectric coolers (TECs) based on the Peltier effect. TECs have exhibited significant advantages compared to conventional vapor-compression refrigeration systems, including small size, free of noise, moving parts, working fluid, and chemical reaction.[58,59]

As demonstrated by these results, this study highlights the synergies between machine learning-enabled Bayesian optimization and expert-driven experimental search. Human intuition is critical to defining the BO problem by identifying the experimental decision variables and their bounds. GPR is especially well-suited for sparse noisy data arising from expensive experiments as GPR "intelligently interpolates" from prior experiments. Early in the experimental campaign, we purposefully explored a mix of BO and human recommended sintering conditions. The latter helped bias the search to consider unexplored regions of the decision space based on prior knowledge. Late in the campaign, we used expert intuition to down select recommended experimental conditions with similar EI scores. We found these strategies to be less cumbersome than designing custom GPR kernels to incorporate said prior knowledge.[40,60] Moreover, this study demonstrates the robustness and flexibility of the GPR strategy, as we successfully extended the GPR input space to include thickness partway through the experimental campaign. While GPR models do not offer full mechanistic insights, analysis of the kernel length scales provides a relative importance of each input variable. We used this information to design one-dimensionally sensitivity analyses near the optimal sintering conditions and perform the corresponding materials characterization to develop a mechanistic understanding of the results (**Figures 2, S5**, **S7**, **S11, S12,**

Tables S2, S3, and S4). Moreover, emerging physics-based machine learning models can be incorporated into the proposed framework. In our opinion, these synergies between machine learning and expert intuition are key factors to success.

4. Conclusion

In summary, we report the first machine learning-assisted ultrafast flash sintering of flexible silver-selenide TE devices for energy harvesting applications. BO significantly accelerated our findings of a set of intense pulsed light (flash) sintering variables leading to an ultrahigh power factor of 2205 $\mu W/mK^2$, and zT of 1.1 at room temperature realized with sintering time less than 1.0 second. Flash sintered films demonstrate outstanding flexibility with 92% retention of the PF after 10^3 bending cycles. The maximum power density of a six-leg TEG is 0.5 and 26.6 mW/cm^2 at ΔT of 10 K and 70 K, respectively. The ultrahigh-performance, low-cost, and highly flexible silver-selenide TE films show great potential for energy harvesting and wearables. Although this study focuses on the optimization of flash sintering for silver-selenide TE materials, this machine learning-assisted experimentation strategy possesses the potential for ultrafast sintering of other TE material systems (e.g., Bi_2Te_3, and Sb_2Te_3) and roll-to-roll manufacturing of a broad range of energy, thermal, and electronic devices.

Materials and Methods

Synthesis of silver-selenide nanostructures

The silver-selenide nanostructures were prepared by bottom-up synthesis approach. Selenium dioxide (2.5 g) and polyvinylpyrrolidone (PVP, 0.05 g) are dissolved in 200 mL deionized water, followed by the addition of 60 mL ethanol to adjust the surface tension of the solution. The above solution was then added dropwise to a stirred solution of ascorbic acid (3.2 wt%, 200 mL) in water, leading to the formation of selenium nanowires (red). After vigorously stirring for 1 h, stoichiometric amount of silver precursor solution ($AgNO_3$ in water) was introduced to the above mixture and left to react overnight. The final product was collected by centrifugation, and then washed with water and ethanol each three times before use.

Characterization

Crystal structures of synthesized nanostructures were examined via X-ray diffractometry (XRD; MiniFlex; Rigaku) using Cu Ka radiations over a 2θ range of 20-60. Microstructures and chemical compositions of the TE films were examined using scanning electron microscopy (Helios G4 Ux Dual Beam) coupled with energy-dispersive X-ray spectrometer (EDS, Bruker).

Flash sintering of silver-selenide films

Flash sintering was performed using a Sinteron 2100 (Xenon Corp., USA) with a 107 mm Xenon spiral lamp. The S-2100 was configured for maximum pulse durations of 3 ms with the sintering carried out in an ambient environment. The S-2100 produced the pulse energy (single) ranging from 30 to 2850 J.

Measurement of TE properties

The room temperature Seebeck coefficient and electrical conductivity are measured using a custom-built setup. We used the four-point probe method for electrical conductivity measurement. To measure the thickness of the films precisely, we used cryogenic cooling of the films by liquid nitrogen to create sharp edge for measuring the thickness using SEM, as shown in **Figure S5**. For Seebeck coefficient measurement, we applied a temperature gradient (6 K) across the film and measured the induced voltage and temperatures using k-type thermocouples. The Seebeck coefficient is calculated as $S = \frac{-\Delta V}{\Delta T}$. The measurement error of the custom-built apparatus was ~5% for both the electrical conductivity, and the Seebeck coefficient. Details of the measurements are described in our previous work.[61] We used the Angstrom method for in-plane thermal conductivity measurement of the silver-selenide films. The room temperature in-plane thermal conductivity κ was determined by measuring the thermal diffusivity α, specific heat capacity c_p, and density ρ, using the relationship $\kappa = \alpha\rho c_p$. Thermal diffusivity was measured using the Angstrom method by applying a sinusoidal heat signal at one end of the sample and measuring the temperature response as a function of time at two different locations along with the sample. **Figure S12** shows the cross-sectional SEM image of the film used for thermal diffusivity measurement. The thermal diffusivities of both the porous filtration membrane and the combined membrane and silver-selenide film are measured. Modified effective medium theory was used to extract the thermal conductivity of the silver-selenide film itself. Details of the measurement process and thermal conductivity extraction are described in Supplementary Information. Thermal conductivity measurement error was estimated around 10%. Specific heat capacity and density values are adopted form a previous report.[57]

Hall effect measurement

The hall effect measurement is conducted to measure the room temperature carrier transport properties of unsintered, and flash sintered silver-selenide films under the optimized condition (experiment 32). **Table S3** shows the carrier mobility (μ) and carrier concentration (n). We used an automatic hall effect measurement system (INSTEC, H8200) for room temperature carrier mobility and concentration measurement. We measured two films (10 mm × 10 mm) for each condition (unsintered and sintered). To minimize the electrical contact resistance between the leads and the film, four corners of the film (100 μm × 100 μm) were sputter coated with a 30 nm layer of 80% Au and 20% Pd.

TEG fabrication and testing

Two thermoelectric generators were assembled with six silver-selenide films sintered under the optimum condition (experiment 32: 2.3 kV voltage, 1.5 ms pulse duration, 4 pulses, and 293 ms pulse delay) on mica and flexible polyimide substrate with 150 μm and 25 μm thickness, respectively. Each leg with a size of 12 mm × 4 mm × 2.5 μm was attached to the substrate using double-sided tape. To minimize the contact resistance, both ends of each film (1 mm × 4 mm) were sputter coated with a 30 nm layer of 80% Au and 20% Pd and then the legs were connected by silver paste (Flash-dry, SPI). We used a custom in-house apparatus for measuring the device performance under different temperature gradients with two k-type thermocouples for measuring cold and hot side temperatures as shown in **Figure S16.**

Design of initial experiments

Special care is required to select the initial training data used for machine learning-based optimization of experiments.[62] In this work, to determine the parameters for Experiments 1 to 6 in **Table S1**, we consider two factors for three sintering variables: voltage (2.2 or 2.4 kV), pulse duration (1 or 2 ms) and number of pluses (1 pulse or 5 pulses with 1000 ms pulse delay). Thickness was held constant. Instead of performing a full factorial design ($2^3 = 8$), we decided to omit the two experiments with 2 ms pulse duration and 5 pulses to avoid burning any samples (based on our prior experience). The data from these first six experiments were used to training the initial machine learning models.

Machine learning and Bayesian optimization

Gaussian Process Regression (GPR) and Bayesian Optimization (BO) are popular machine learning techniques to intelligently improve expensive experiments through adaptive learning. In this section, we describe the underlying mathematics behind GPR and BO and emphasize specific details for implementation with TE materials.

Let $f(\boldsymbol{x})$ represent unknown function that maps experiment conditions $\boldsymbol{x}$ (input, vector) and power factor y (output, scalar). Mathematically, we seek to solve the optimization problem $\max_{\boldsymbol{x}\epsilon\boldsymbol{X}} f(\boldsymbol{x})$, where the set $\boldsymbol{X}$ contains all possible (feasible) experiment conditions. However, experiments are expensive and time-consuming. BO recommends a sequence of experiments to maximize power factor using three main steps: first the GPR machine learning model is training on available data to emulate the unknown function $f(\boldsymbol{x})$. Second, decision theory is used to recommend the most valuable experiments; third, the proposed experiments are conducted, measured, and recorded. The process is repeated multiple times until the desired power factor is obtained or the experimental budget is exhausted.

A single flash sintering experiment requires specifying five input variables – voltage (x_{i1}), pulse duration (x_{i2}), pulse delay (x_{i3}), number of pulses (x_{i4}), and thickness (x_{i5}) – which result in a correspond power factor (y_i). Here the subscript i denotes the experiment (sample) number. All samples are combined for the dataset $D = \{(\boldsymbol{x}_i,y_i),|\boldsymbol{x}_i \in \mathbb{R}^5, y_i \in \mathbb{R}, i \in 1,...,N\}$, abbreviated as $D = (\boldsymbol{X},\boldsymbol{y})$.

We now construct a GPR model to predict the outcome of a new experiment, $f(\boldsymbol{x}_*)$, at conditions $\boldsymbol{x}_*$. GPR is a non-parametric model, which means the data D are directly embedded into the model. The GPR model is fully specified by the dataset D, the mean function $m(X)$, and the kernel (covariance) function $K(\boldsymbol{X},\boldsymbol{X}')$. In this work, we use the radial basis function as the kernel $k_{RBF}(\boldsymbol{x}, \boldsymbol{x}'|\boldsymbol{l}) = e^{-\frac{1}{2}\sum_{j=1}^{5}\left(\frac{x_j - x'_j}{l_j}\right)^2}$, which measures the distance between each pair of experiment condition $\boldsymbol{x}$ and $\boldsymbol{x}'$. Thus, when making a prediction at the new condition experimental $\boldsymbol{x}_*$, the GPR incorporates all information from dataset D using the kernel to "weight" the importance of all prior experiments using the distance between $\boldsymbol{x}_*$ and all $\boldsymbol{x}_i \in D$. In this way, the GPR is a sophisticated ML approach to interpolate between all prior experiments in D without requiring an assumed parametric model to map inputs $\boldsymbol{x_i}$ to output y. Instead, the GPR model assumes the experimental outcomes are described by a multivariate normal distribution $\boldsymbol{N}(.,.)$:

$$\begin{bmatrix} \boldsymbol{f}(\boldsymbol{X}) \\ f(\boldsymbol{x}_*) \end{bmatrix} \sim \boldsymbol{N}\left(\begin{bmatrix} \boldsymbol{m}(\boldsymbol{X}) \\ m(\boldsymbol{x}_*) \end{bmatrix}, \begin{bmatrix} \boldsymbol{K}(\boldsymbol{X},\boldsymbol{X}) & \boldsymbol{K}(\boldsymbol{X},\boldsymbol{x}_*) \\ \boldsymbol{K}(\boldsymbol{x}_*,\boldsymbol{X}) & \boldsymbol{K}(\boldsymbol{x}_*,\boldsymbol{x}_*) \end{bmatrix}\right) \quad \#(1)$$

Applying Bayes rule of probability gives the following analytical expressions for the prediction mean and variance at new experimental condition $\boldsymbol{x}_*$: [63]

$$\mu_*(\boldsymbol{x}_*) = E(f(x_*)|\boldsymbol{y}) = \boldsymbol{m}(\boldsymbol{x}_*) + \boldsymbol{K}(\boldsymbol{x}_*,\boldsymbol{X})[\boldsymbol{K}(\boldsymbol{X},\boldsymbol{X}) + \sigma^2\boldsymbol{I}]^{-1}(\boldsymbol{y} - \boldsymbol{m}(\boldsymbol{X}))\#(2a)$$

$$\sigma_*(\boldsymbol{x}_*) = Var(f(x_*)|\boldsymbol{y}) = \boldsymbol{K}(\boldsymbol{x}_*,\boldsymbol{x}_*) - \boldsymbol{K}(\boldsymbol{x}_*,\boldsymbol{X})[\boldsymbol{K}(\boldsymbol{X},\boldsymbol{X}) + \sigma^2\boldsymbol{I}]^{-1}\boldsymbol{K}(\boldsymbol{X},\boldsymbol{x}_*)\#(2b)$$

Eq. (2) also includes normally distributed observation error with mean zero and variance σ^2. The hyperparameters $\boldsymbol{l} = (l_1, l_2, l_3, l_4, l_5)^T$ in kernel function $k_{RBF}(\boldsymbol{x}, \boldsymbol{x}')$, also called length-scales, determines the importance of the features. If length-scale l_j is small, then the corresponding feature $\boldsymbol{x}_j$ is more important to predict the output y. Optimal length-scales are computed by maximizing log marginal likelihood (LML).[60]

Expected Improvement (EI) in popular acquisition function to recommend an optimal $\boldsymbol{x}_*$ in a BO framework. EI balances the trade-offs between exploration, i.e., choosing $\boldsymbol{x}_*$ in regions with high uncertainty, and exploitation, i.e., choosing $\boldsymbol{x}_*$ in regions that will maximize $f(\boldsymbol{x}_*)$. EI achieves this balance by computing the expected value of the improvement between $f(\boldsymbol{x}_*)$ and $f(\boldsymbol{x}^+)$, where $\boldsymbol{x}^+$ is the experiment condition in dataset D that has highest power factor. Thus mathematically $EI(\boldsymbol{x}_*) = \max\left(f(\boldsymbol{x}_*) - f(\boldsymbol{x}^+), 0\right)$. By exploiting mathematical properties of the normal distribution, $EI(\boldsymbol{x})$ has the following analytic formula:

$$EI(\boldsymbol{x}_*) = \begin{cases} \left(\mu_*(\boldsymbol{x}_*) - f(\boldsymbol{x}^+)\right)\Phi(z) + \sigma_*(\boldsymbol{x}_*)\phi(z), & \sigma_*(\boldsymbol{x}_*) > 0 \\ 0, \ \text{otherwise} \end{cases} \#(3a)$$

$$z(\boldsymbol{x}_*) = \begin{cases} \dfrac{\left(\mu_*(\boldsymbol{x}_*) - f(\boldsymbol{x}^+)\right)}{\sigma_*(\boldsymbol{x}_*)}, & \sigma_*(\boldsymbol{x}_*) > 0 \\ 0, \ \text{otherwise} \end{cases} \#(3b)$$

Here, $\Phi(\cdot)$ is cumulative distribution function, and $\phi(\cdot)$ is probability density function, respectively, for the standard normal distribution. The GPR and BO workflows were implemented in Scikit-learn.[64] The entire workflow, including the interaction between BO and human experts (experimentalist), is illustrated in **Figure 7.** The entire procedure including hypertuning training and EI optimization requires less than 2 minutes on a MacBook with a 2.6 GHz Intel Core i7 CPU.

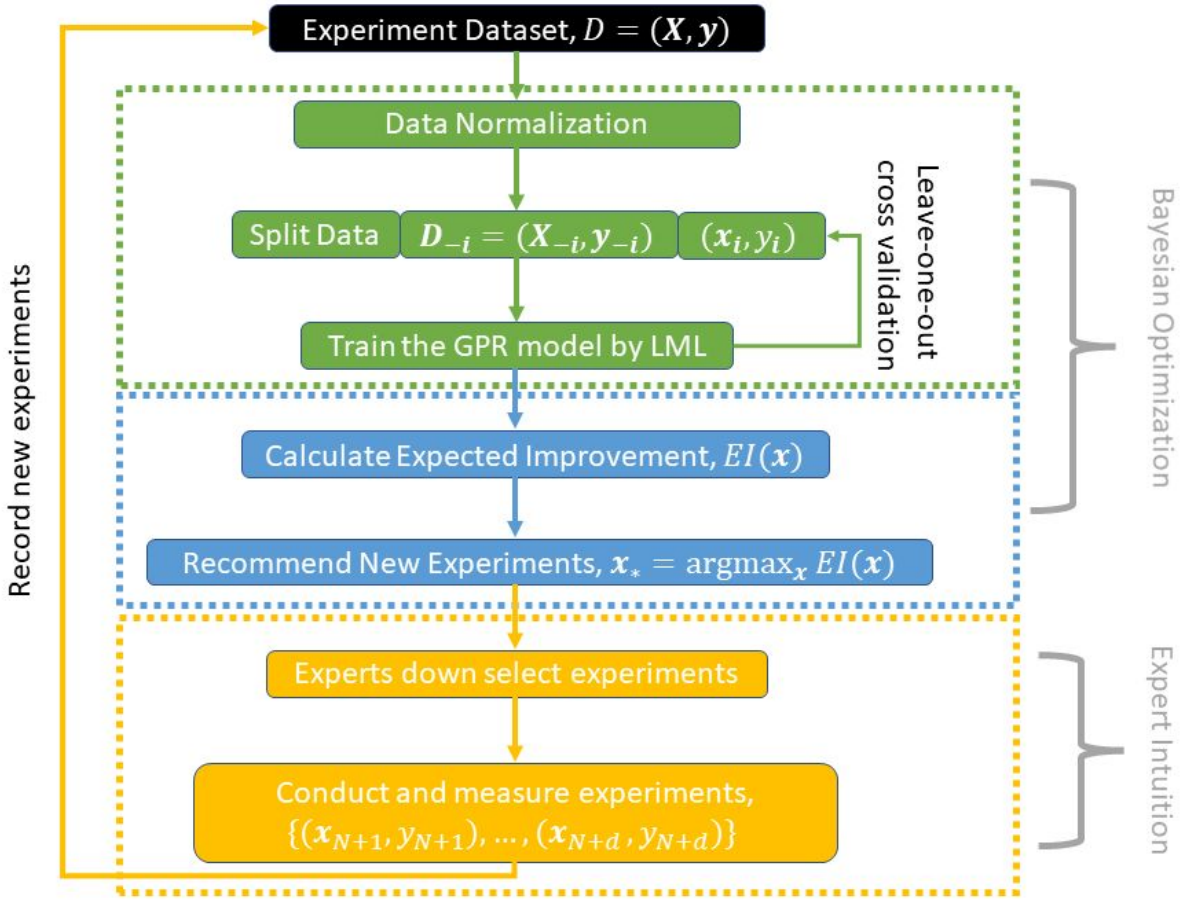

Figure 7. The proposed workflow integrates Bayesian optimization (BO) and human intuition. The overall procedure contains three steps: Gaussian process regression (GPR) model training (green box), expected improvement (EI) calculation (blue box), and experimentalist down selection and fabrication (yellow box). The BO is implemented in first two steps and expert intuition is incorporated in the last one. The dataset, $D = (\boldsymbol{X}, \boldsymbol{y})$, contains N samples of recorded sintering variables $\boldsymbol{x}_i$, which consist of voltage (x_{i1}), pulse duration (x_{i2}), pulse delay (x_{i3}), number of pulses (x_{i4}), and thickness (x_{i5}), and the corresponding power factor(y_i). In each iteration, dataset D is provided to BO, and d new experiments, $\{(x_{N+1}, y_{N+1}), \ldots, (x_{N+d}, y_{N+d})\}$, are selected by human intuition, performed, and added to dataset D; the procedure terminates when the expected improvement approaches zero or the experimental budget is exhausted.

5. Acknowledgements

We would like to acknowledge support from the U.S. Department of Energy under awards DE-EE0009103. Y. Z. would like to acknowledge funding support from the National Science Foundation under award CMMI-1747685 and the U.S. Department of Energy under award DE-NE0008812.

6. References

1 J. Liang, T. Wang, P. Qiu, S. Yang, C. Ming, H. Chen, Q. Song, K. Zhao, T.-R. Wei, D. Ren, Y.-Y. Sun, X. Shi, J. He and L. Chen, *Energy & Environmental Science*, 2019, **12**, 2983–2990.

2 B. Lee, H. Cho, K. T. Park, J.-S. Kim, M. Park, H. Kim, Y. Hong and S. Chung, *Nature Communications*, 2020, **11**.

3 A. Nozariasbmarz, H. Collins, K. Dsouza, M. H. Polash, M. Hosseini, M. Hyland, J. Liu, A. Malhotra, F. M. Ortiz, F. Mohaddes, V. P. Ramesh, Y. Sargolzaeiaval, N. Snouwaert, M. C. Özturk and D. Vashaee, *Applied Energy*, 2020, **258**, 114069.

4 M. Dargusch, W. D. Liu and Z. G. Chen, *Advanced Science*, 2020, **7**, 2001362.

5 S. Masoumi, S. O. Shaughnessy and A. Pakdel, *Nano Energy*, 2022, **92**, 106774.

6 G. J. Snyder and E. S. Toberer, *Nat. Mater.*, 2008, **7**, 105–114.

7 M. He, F. Qiu and Z. Lin, *Energy & Environmental Science*, 2013, **6**, 1352.

8 Y. Du, S. Z. Shen, K. Cai and P. S. Casey, *Prog. Polym. Sci.*, 2012, **37**, 820–841.

9 H. Goldsmid, *Materials*, 2014, **7**, 2577–2592.

10 I. T. Witting, T. C. Chasapis, F. Ricci, M. Peters, N. A. Heinz, G. Hautier and G. J. Snyder, *Advanced Electronic Materials*, 2019, **5**, 1800904.

11 Y. Lu, Y. Qiu, K. Cai, Y. Ding, M. Wang, C. Jiang, Q. Yao, C. Huang, L. Chen and J. He, *Energy & Environmental Science*, 2020, **13**, 1240–1249.

12 C. Jiang, P. Wei, Y. Ding, K. Cai, L. Tong, Q. Gao, Y. Lu, W. Zhao and S. Chen, *Nano Energy*, 2021, **80**, 105488.

13 C. Jiang, Y. Ding, K. Cai, L. Tong, Y. Lu, W. Zhao and P. Wei, *ACS Applied Materials & Interfaces*, 2020, **12**, 9646–9655.

14 P. Jood, R. Chetty and M. Ohta, *Journal of Materials Chemistry A*, 2020, **8**, 13024–13037.

15 S. Jo, S. Cho, U. J. Yang, G. S. Hwang, S. Baek, S. H. Kim, S. H. Heo, J. Y. Kim, M. K. Choi and J. S. Son, *Advanced Materials*, 2021, **33**, 2100066.

16 J. A. Perez-Taborda, O. Caballero-Calero, L. Vera-Londono, F. Briones and M. Martin-Gonzalez, *Advanced Energy Materials*, 2017, **8**, 1702024.

17 Q. Gao, W. Wang, Y. Lu, K. Cai, Y. Li, Z. Wang, M. Wu, C. Huang and J. He, *ACS Applied Materials & Interfaces*, 2021, **13**, 14327–14333.

18 S. Hou, Y. Liu, L. Yin, C. Chen, Z. Wu, J. Wang, Y. Luo, W. Xue, X. Liu, Q. Zhang and F. Cao, *Nano Energy*, 2021, **87**, 106223.

19 Y. Li, Q. Lou, J. Yang, K. Cai, Y. Liu, Y. Lu, Y. Qiu, Y. Lu, Z. Wang, M. Wu, J. He and S. Shen, *Advanced Functional Materials*, 2021, **32**, 2106902.

20 Y. Ding, Y. Qiu, K. Cai, Q. Yao, S. Chen, L. Chen and J. He, *Nature Communications*, 2019, **10**.

21 M. Oghbaei and O. Mirzaee, *Journal of Alloys and Compounds*, 2010, **494**, 175–189.

22 L. Shi, M. Layani, X. Cai, H. Zhao, S. Magdassi and M. Lan, *Sensors and Actuators B: Chemical*, 2018, **256**, 938–945.

23 J. Xi, K. Xi, A. Sadhanala, K. H. L. Zhang, G. Li, H. Dong, T. Lei, F. Yuan, C. Ran, B. Jiao, P. R. Coxon, C. J. Harris, X. Hou, R. V. Kumar and Z. Wu, *Nano Energy*, 2019, **56**, 741–750.

24 D. Dudina, B. Bokhonov and E. Olevsky, *Materials*, 2019, **12**, 541.

25 R. R. Mishra and A. K. Sharma, *Composites Part A: Applied Science and Manufacturing*, 2016, **81**, 78–97.

26 W. Mi, P. Qiu, T. Zhang, Y. Lv, X. Shi and L. Chen, *Applied Physics Letters,* 2014, **104**, 133903.

27 T. Mineta, T. Saito, T. Yoshihara and H. Sato, *Materials Science and Engineering: A*, 2019, **754**, 258–264.

28 E. B. Secor, T. Z. Gao, M. H. Dos Santos, S. G. Wallace, K. W. Putz and M. C. Hersam, *ACS Applied Materials & Interfaces*, 2017, **9**, 29418–29423.

29 Y. Galagan, E. W. C. Coenen, R. Abbel, T. J. van Lammeren, S. Sabik, M. Barink, E. R. Meinders, R. Andriessen and P. W. M. Blom, *Organic Electronics*, 2013, **14**, 38–46.

30 M. Hösel and F. C. Krebs, *Journal of Materials Chemistry*, 2012, **22**, 15683.

31 S. Norita, D. Kumaki, Y. Kobayashi, T. Sato, K. Fukuda and S. Tokito, *Organic Electronics*, 2015, **25**, 131–134.

32 M. Saeidi-Javash, W. Kuang, C. Dun and Y. Zhang, *Advanced Functional Materials*, 2019, **29**, 1901930.

33 T. Wang, C. Zhang, H. Snoussi and G. Zhang, *Advanced Functional Materials*, 2019, **30**, 1906041.

34 Z. Hou, Y. Takagiwa, Y. Shinohara, Y. Xu and K. Tsuda, *ACS Applied Materials & Interfaces*, 2019, **11**, 11545–11554.

35 Y. Iwasaki, I. Takeuchi, V. Stanev, A. G. Kusne, M. Ishida, A. Kirihara, K. Ihara, R. Sawada, K. Terashima, H. Someya, K.-ichi Uchida, E. Saitoh and S. Yorozu, *Scientific Reports*, 2019, **9**.

36 C. Tian, T. Li, J. Bustillos, S. Bhattacharya, T. Turnham, J. Yeo and A. Moridi, *Advanced Intelligent Systems*, 2021, **3**, 2100014.

37 C. Wang, X. P. Tan, S. B. Tor and C. S. Lim, *Additive Manufacturing*, 2020, **36**, 101538.

38 T. Erps, M. Foshey, M. K. Luković, W. Shou, H. H. Goetzke, H. Dietsch, K. Stoll, B. von Vacano and W. Matusik, *Science Advances*, 2021, **7**.

39 R.-R. Griffiths and J. M. Hernández-Lobato, *Chemical Science*, 2020, **11**, 577–586.

40 K. Wang and A. W. Dowling, *Current Opinion in Chemical Engineering*, 2022, **36**, 100728.

41 U. Erturun, K. Erermis and K. Mossi, *Applied Energy*, 2015, **159**, 19–27.

42 A. Kumar, K. Singh and R. Das, *Applied Thermal Engineering*, 2019, **159**, 113935.

43 A. Kanatzia, C. Papageorgiou, C. Lioutas and T. Kyratsi, *Journal of Electronic Materials*, 2012, **42**, 1652–1660.

44 R. B. Gramacy, *Surrogates: Gaussian process modeling, design, and optimization for the Applied Sciences*, CRC Press, Taylor & Francis Group, Boca Raton, FL, 2020.

45 J. Recatala-Gomez, A. Suwardi, I. Nandhakumar, A. Abutaha and K. Hippalgaonkar, *ACS Applied Energy Materials*, 2020, **3**, 2240–2257.

46 C. Zeng, W. Zhang, S. Ding, Z. Yang, H. Zeng and Z. Li, *CrystEngComm*, 2013, **15**, 5127.

47 P. Jood, R. Chetty and M. Ohta, *Journal of Materials Chemistry A*, 2020, **8**, 13024–13037.

48 C. Lee, Y.-H. Park and H. Hashimoto, *Journal of Applied Physics*, 2007, **101**, 024920.

49 F. F. Aliev, M. B. Jafarov and V. I. Eminova, *Semiconductors*, 2009, **43**, 977–979.

50 M. Ferhat and J. Nagao, *Journal of Applied Physics*, 2000, **88**, 813–816.

51 L. Ward, A. Agrawal, A. Choudhary and C. Wolverton, *npj Computational Materials*, 2016, **2**.

52 T. Varghese, C. Dun, N. Kempf, M. Saeidi-Javash, C. Karthik, J. Richardson, C. Hollar, D. Estrada and Y. Zhang, *Advanced Functional Materials*, 2019, **30**, 1905796.

53 C. Dun, W. Kuang, N. Kempf, M. Saeidi-Javash, D. J. Singh and Y. Zhang, *Advanced Science*, 2019, **6**, 1901788.

54 E. Jin Bae, Y. Hun Kang, K.-S. Jang and S. Yun Cho, *Scientific Reports*, 2016, **6**.

55 H. Wang, S.-in Yi, X. Pu and C. Yu, *ACS Applied Materials & Interfaces*, 2015, **7**, 9589–9597.

56 S. J. Kim, J. H. We and B. J. Cho, *Energy & Environmental Science*, 2014, **7**, 1959.

57 J. Gao, L. Miao, H. Lai, S. Zhu, Y. Peng, X. Wang, K. Koumoto and H. Cai, *iScience*, 2020, **23**, 100753.

58 W. Y. Chen, X. L. Shi, J. Zou and Z. G. Chen, *Small Methods*, 2022, **6**, 2101235.

59 S. H. Zaferani, M. W. Sams, R. Ghomashchi and Z.-G. Chen, *Nano Energy*, 2021, **90**, 106572.

60 C. M. Bishop, Pattern recognition and machine learning, Springer New York, New York, NY, 2016.

61 M. Zeng, H. Xie, M. Saeidi-Javash, A. N. M. Tanvir, Y. Du, J. Chen, M. G. Kanatzidis and Y. Zhang, *Journal of Materials Chemistry A*, 2021, **9**, 22555–22562.

62 B. Cao, L. A. Adutwum, A. O. Oliynyk, E. J. Luber, B. C. Olsen, A. Mar and J. M. Buriak, *ACS Nano*, 2018, **12**, 7434–7444.

63 Günter A., R. Kruse and B. Neuman, in Ki 2003: Advances in artificial intelligence: 26th annual German conference on AI, ki 2003, Hamburg, Germany, September 15-18, 2003: Proceedings, Springer, Berlin, 2003.

64 F. Pedregosa, G. Varoquaux, A. Gramfort, V. Michel, B. Thirion, O. Grisel, M. Blondel, P. Prettenhofer, R. Weiss, V. Dubourg, J. Vanderplas, A. Passos, D. Cournapeau, M. Brucher, M. Brucher and E. Duchesnay, *Journal of Machine Learning Research*, 2011, **12**, 2825–2830.